Symmetric coalescence of two hydraulic fractures

Niall J. O'Keeffe[a,1], **Zhong Zheng**[a,b], **Herbert E. Huppert**[a], **and P. F. Linden**[a]

[a]Department of Applied Mathematics and Theoretical Physics, University of Cambridge, Cambridge, CB3 0WA, UK; [b]BP Institute and Department of Earth Sciences, University of Cambridge, Cambridge CB2 3EQ, UK

This manuscript was compiled on October 10, 2018

The formation of a fracture network is a key process for many geophysical and industrial practices from energy resource recovery to induced seismic management. We focus on the initial stage of a fracture network formation, employing experiments on the symmetric coalescence of two equal coplanar, fluid-driven penny-shaped fractures in a brittle elastic medium. Initially, the fractures propagate independently of each other. The fractures then begin to interact and coalesce, forming a bridge between them. Within an intermediate period following the initial contact, most of the fracture growth is localised along this bridge, perpendicular to the line connecting the injection sources. Using light attenuation and particle image velocimetry to measure both the fracture aperture and velocity field, and characterise the growth of this bridge. We model this behaviour using a geometric volume conservation argument, dependent on the symmetry of the interaction, with a two-dimensional approximation for the bridge. We also verify experimentally the scalings for the bridge growth and the shape of the thickness profile along the bridge. The influence of elasticity and toughness of the solid, injection rate of the fluid and initial location of the fractures are captured by our scaling.

Hydraulic Fracturing | Hydrogel | Coalescence

Fluid-driven fracturing involves the propagation of a fracture within a solid due to pressure applied by a fluid. This technique has predominantly been used in unconventional energy reservoirs with low permeabilities that make the resource difficult to extract (1). The creation of fractures increases the overall permeability of the rock formation, providing easier paths for hydrocarbons to escape. Individual fractures within these formation networks can interact with each other by coalescing and altering propagation directions, which will have a large influence of the success of an operation. Other applications that may include similar coalescence dynamics are measurement of existing (*in-situ*) stresses (2), carbon sequestration (3), geothermal energy recovery (4), magma transport (5), compensation grouting (6), and disposal of liquid waste underground.

Recent experimental studies on single penny-shaped fractures successfully captured the dynamic behaviours for the propagation under two different dominant energy dissipation mechanisms, viscous dissipation and material toughness (7–9). In this paper we focus on the coalescence of two fluid-driven penny-shaped fractures when the fracture is dominated by the material toughness, and provide experimental observations and scaling arguments on the dynamic behaviour during the growth of bridges formed between two fractures. While the experiments and model are simplifications of the practical applications, the understanding of the physical mechanisms of fracture coalescence provides new insights into the initial stage of fracture network formation and may have implications in some of the applications previously noted.

Experimental Setup

In order to investigate the coalescence of hydraulic fractures, we designed a dual-fracturing experimental setup, which consists of two injection needles with radii of 0.81 mm set in a polyacrylamide hydrogel of dimensions $100 \times 100 \times 77$ mm (Fig. 1). Four polycarbonate plates of 1 mm were introduced into the sides of the acrylic container to impose a small initial principal stress perpendicular to the needle, which sets the direction of fracture propagation. The plates ensured that the two tensile fractures coalesced approximately on the same plane, as long as the needle positions were fixed to the same depth into the gel. The two needles were placed a distance l_0 apart. This distance l_0 (30–40 mm) was sufficiently large so that any rapid fracture due to initiation (radius $\lesssim 5$ mm) around the needle tip did not influence the dynamics of coalescence; l_0 was also chosen to be sufficiently small so that finite container did not affect fracture propagation.

The hydrogels used in the experiments were transparent, enabling detailed optical measurements. They were also brittle and elastic, allowing significant variation in both Young's modulus E and fracture toughness K (10). Newtonian fluids, water–glycerin mixtures with different dynamic viscosities μ, were injected at constant volumetric rates Q_0 into the hydrogel using a syringe pump (HA PhD Ultra). The experimental parameters (see methods) were chosen so that the fractures propagated in the toughness-dominated regime before coalescence (7, 9, 11).

Mathematical Model and Experimental Results

A representative time evolution of the interaction between the two fractures is shown in Fig. 2. Initially, the two fractures propagated independently of each other as standard penny-

Significance Statement

We present an experimental investigation on the coalescence of hydraulic fractures in a brittle solid. Using a dual-fracturing setup, we obtain high-resolution experimental measurements on the time evolution of the fracture profiles and internal velocity field before, during and after fracture coalescence. These measurements demonstrate an intermediate time of coalescence during the dynamic interaction of two fractures. The work probes the dynamic formation of a fracture network, which is crucial to the industrial practice of energy resource recovery, compensation grouting, and the reservoir integrity of many confined systems involving fluid injection.

Author contributions: N.J.O.K., Z.Z., H.E.H. and P.F.L. designed research. N.J.O.K. performed research. N.J.O.K. and Z.Z. analysed data. N.J.O.K., Z.Z., P.F.L. and H.E.H. wrote the paper.

The authors declare no conflict of interest.

[1]To whom correspondence should be addressed. E-mail: okeeffen@damtp.cam.ac.uk

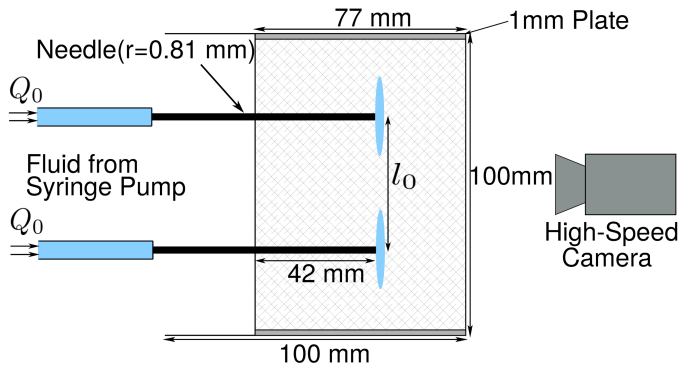

Fig. 1. Schematic of the dual-fracturing experimental apparatus. Fluid is injected from two separate syringes on a dual-syringe pump to ensure an equal injection rate into each fracture, both of which are generated on the same plane.

shaped fractures in the x-y plane, where the injection needles are aligned along the x axis, and the distance between the fractures gradually reduced (Fig. 2a). When the fractures were sufficiently close, the stress intensity in the hydrogel increased significantly at the inner crack tip nearest to the other fracture (13), which caused the fractures to become attracted to each other. This attraction retards the outer radial growth of each fracture and induces propagation only in the direction of the other cavity, causing coalescence.

The fractures were observed to coalesce and form a narrow bridge at a particular time (which we denote by $t = 0$). Shortly after coalescence, we observed that significant fracture growth only occurred in the region close to the bridge, which caused a rapid growth of this bridge (Fig. 2b). When the bridge length $2d$ became comparable to the diameter $2R_0$ of each fracture, growth spread to the entire envelope of the two interacting fractures. As time progressed the two fractures gradually became indistinguishable, and approached the shape of a standard single radial fracture in the toughness dominated regime (with injection rate $2Q_0$). Particle image velocimetry (PIV) measurements are provided for each stage of the fracturing and coalescing process in Figs. 2a-e. We can see from Fig. 2a that initially the flow was mostly radial, similar to that observed for single fractures (7). Then once the fractures coalesced, the flow everywhere was attracted towards the bridge and a large increase in velocity occurred in the vicinity of the bridge (Fig. 2b). After this initial spike in velocity and as the bridge began to grow, a stagnation point appeared in the centre of this bridge, with velocity vectors pointing along the bridge in the y direction towards its edges (Figs. 2c-e).

In Figs. 2f and 2g we can see the evolution of coalescence along the x-z plane, where the fracture is assumed to be symmetric about its mid-plane. Shortly after the cracks first touched, the profile in this plane centred at the point of coalescence can be seen to level out quickly. A three dimensional image of the bridge at a particular time is also shown in figure 3, where the full shape of the bridge and its roughness can be seen.

Mathematical Model. The interface shape in the x-y plane motivates us to explore the behaviour for the growth of the bridge shortly after the coalescence of two fractures. In particular, we investigate the growth of the bridge length $2d$, employing a volume conservation argument surrounding a local region at the point of coalescence (14–18). We consider a box around the bridge of volume V (Fig. 2c), with length $2d$, width $2b$ and height h. Assuming the individual fractures are circular, geometry implies that $b = R_0 - \left(R_0^2 - d^2\right)^{1/2} \approx d^2/2R_0$, provided $d \gg b$. Thus, the volume of this box is $V \approx 4dbh \approx 2d^3h/R_0$. The PIV experiments further illustrate that after a very brief initial increase, the flow rate into either side of the box settles to a constant value and is approximately the imposed injection rate Q_0 (Fig. 4). It follows that

$$\frac{\mathrm{d}V}{\mathrm{d}t} \approx \frac{2d^3h}{R_0 t} \approx 2Q_0, \qquad [1]$$

which provides the scaling relation for the length of the bridge

$$d \approx \left(\frac{Q_0 R_0}{h}\right)^{1/3} t^{1/3}. \qquad [2]$$

Note that the scaling relation (2) is dependent on the height h of the bridge. Consequently, in order to obtain a relationship for the bridge height evolution with time, we further assume that the bridge section can be approximated as a two dimensional fracture. The pressure p inside the two-dimensional fracture is $p \approx E'h/d$, where $E' = E/(1-\nu^2)$ is the plane strain modulus and ν is the Poisson ratio (19). Assuming that the dominant energy dissipation mechanism for the growth of the bridge is through fracture tip opening rather than viscous dissipation, the fracture propagation condition yields $pd^{1/2} \approx K$, where $K = \sqrt{2\gamma_s E'}$ is the material toughness and γ_s is the fracture surface energy of the material (11). Combining this propagation condition, the pressure relation $p \approx E'h/d$ and the mass balance equation (1), we establish the following scaling relations for the bridge length and height

$$d \approx \left(\frac{Q_0 R_0 E'}{K}\right)^{2/7} t^{2/7} \quad \text{and} \quad h \approx \left(\frac{Q_0 R_0 K^6}{E'^6}\right)^{1/7} t^{1/7}. \qquad [3]$$

Equation (3) incorporates the influence of fluid injection rate Q_0, the Young's modulus E and material toughness K of the solid and the distance $2R_0$ between the fracture centres at the moment of coalescence.

Experimental Results. The experimental measurements of the bridge length $2d$ for various parameters are plotted in Fig. 5a. We further rescale the raw data for d based on the bridge scaling equation (3), which leads to a convincing collapse onto a single curve in Fig. 5b. The best power-law fit $d = \alpha_1 (Q_0 R_0 E'/K)^{2/7} t^{\beta_1}$ through the rescaled data during times when $d \lesssim R_0$ after coalescence provides a dimensionless prefactor of $\alpha_1 = 0.81 \pm 0.07$ and exponent $\beta_1 = 0.31 \pm 0.02$. Similarly, we can analyse the experimental data for the bridge height growth at the point of coalescence in Fig. 5c. We measure h by using a 10 pixel average around the point of coalescence. Scaling the data according to equation (3), we again obtain a reasonable collapse (Fig. 5d). The best fit has the form $h = \alpha_2 (Q_0 R_0 K^6/E'^6)^{1/7} t^{\beta_2}$. Fitting this form for early times of bridge growth, we obtain $\alpha_2 = 2.5 \pm 0.2$ and exponent $\beta_2 = 0.14 \pm 0.03$. The data collapse in both d and h, and the agreement of the fitting exponents, within error bounds, with the theoretical values in (3) indicate that we have successfully captured the initial bridge formation process during the fracture-coalescence experiments.

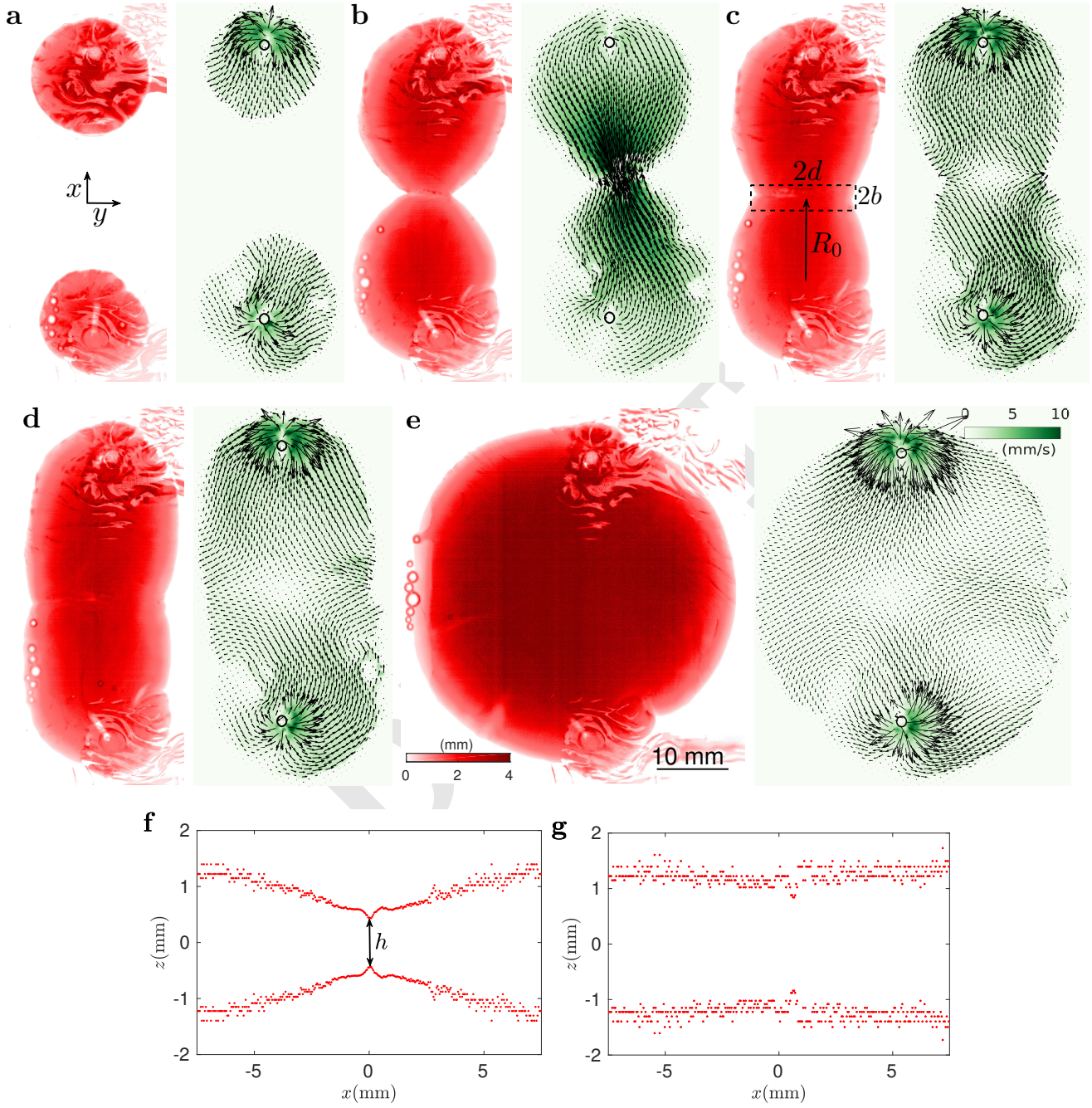

Fig. 2. Time evolution of the coalescence process of two fractures: **a-e**, top-view images and **f-g**, side-view images. The time at which each image was taken is **a**, $t = -6$ s; **b**, $t = 0.01$ s; **c**, $t = 0.8$ s; **d**, $t = 2.5$ s; **e**, $t = 21$ s; **f**, $t = 0.04$ s; and **g**, $t = 0.6$ s. The noise in **f** and **g** is an artefact of the calibration. Both light attenuation (Exp1) and PIV (Exp6) measurements are employed (but not simultaneously for the same experiment), and in **a** to **e** we show the fracture thickness and velocity field from two repeated experiments at the same time. The distortion of light in the dyed images is due to the presence of injection tubes connected to the syringe pump. The colourbar of the PIV images correspond to the velocity magnitude and values shown in (b) are 4 times that in other top-view images.

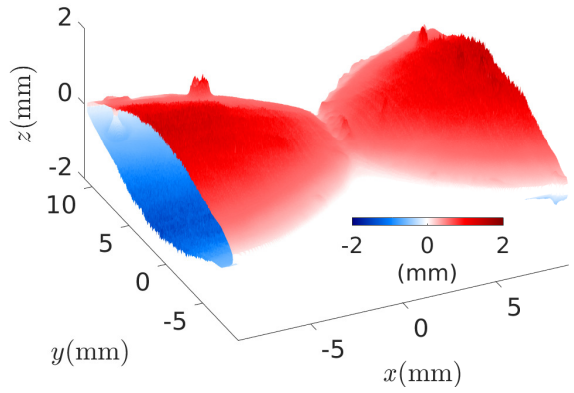

Fig. 3. Three dimensional image of the bridge formed during the coalescence of two fractures in Exp1 at $t = 0.04$.

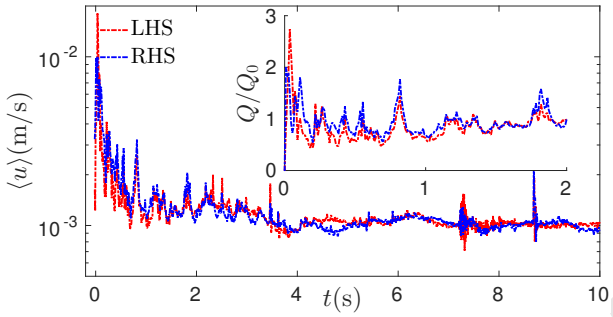

Fig. 4. Measured velocity into either side of the bridge box (Exp6). Inset: a representative computed volume flux value into each side of the bridge box is constant and approximately Q_0, the imposed injection rate (see S.I.).

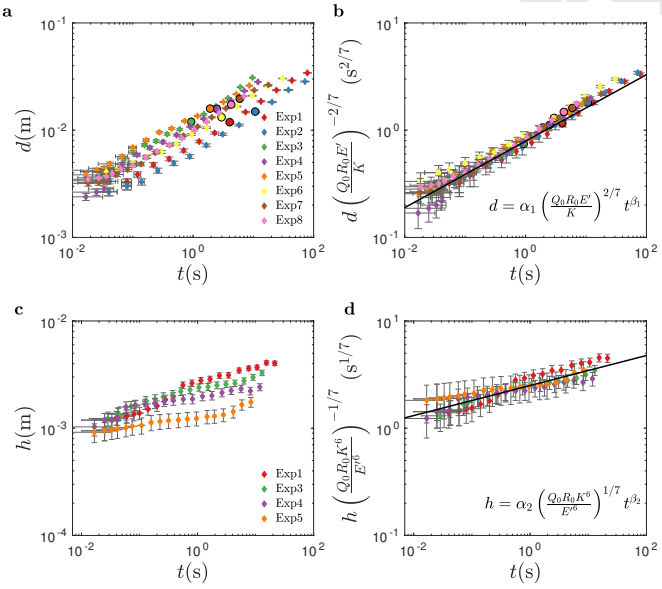

Fig. 5. Experimental measurements of the half bridge length d and height h as a function of time: **a**, raw data of d; **b**, rescaled data of d according to (3); **c**, raw data of h; **d**, rescaled data of h using (3). The points where $d \approx R_0$ are denoted by the circular markers in **a** and **b**. The data collapse in **b** and **d** indicates that the scaling argument (3) captures the fracture coalescence dynamics. In addition, power-law fit provides $\alpha_1 = 0.81 \pm 0.07$, $\beta_1 = 0.31 \pm 0.02$, $\alpha_2 = 2.5 \pm 0.24$ and $\beta_2 = 0.14 \pm 0.03$: The scaling exponents are also consistent with (3).

The height profile along the bridge in the y-z direction is shown in Fig. 6a. Using the toughness height scaling equation (3), we collapse the thickness profiles at different times to a single elliptical shape (Fig. 6b), which provides further evidence that the major resistance for bridge growth in our experiments is dominated by fracture tip opening. The time evolution of the profile shape is further examined in this initial stage of coalescence in Fig. 7a, where $d_s(x,t)$ represents the profile shape above the line $y = 0$ connecting the injection points and hence $d(t) = d_s(0,t)$. The shape evolution also suggests a local universal behaviour: rescaling the data using the geometric relationship leads to good data collapse around the minimum (Fig. 7b).

We note that the resistance for the bridge growth is dominated by material toughness in these experiments. We anticipate the existence of another regime when the dominant energy dissipation mechanism is viscous drag, which is currently under investigation. We also note that at very late times, the coalescing hydraulic fractures fully merge and propagate as a single penny-shaped fracture, with a radius growing according to $\propto t^{2/5}$ in the toughness regime (see S.I.).

Conclusions

To summarise, we investigated experimentally the coalescence of two coplanar penny-shaped hydraulic fractures. In particular, we focused on the early stage of coalescence when two fractures touch each other to form a bridge. We identified the dynamics of the bridge formation process, which provides a novel aspect involved in the formation of a fracture network. Our study addresses a key understudied facet of a wide range of practical applications in the recovery of subsurface energy resources, such as shale gas and geothermal energy, and induced seismic management from fracturing projects. We also note that heterogeneity is common in many of these applications and this may have a significant effect on some of the dynamics observed, which provides a direction for future investigation.

Materials and Methods

Experimental parameters. The experimental parameters used in this paper for each experiment are located in Table 1. The distance between the injection points l_0 was varied between 30 and 40 mm. The Young's modulus E was changed by approximately a factor of 3 from 97 to 320 kPa. The viscosity of the injected fluid μ ranged from 0.28 to 1.13 Pa·s, approximately a factor of 4. The volumetric injection rate Q_0 also varied by an order of magnitude from 2.0 to 20 mL/min. The upper constraints of the injection rate for a given fluid viscosity were mainly imposed by the strength of the syringe pump. For the case of a single fracture, the transition time scale $t_{mk} = (\mu^5 Q_0^3 E'^{13}/K^{18})^{1/2}$ varies between 10^{-6} and 10^{-4} s for these particular experiments, verifying that it is in the toughness regime pre-coalescence.

Experiments 1-5 use light attenuation and experiments 6-8 use PIV measurements. All measurements are taken using a high speed camera (Dalsa Falcon 2 4MP), with a spatial resolution of 1 pixel ≈ 0.037 mm, and frames per second ranging between 60-120 depending on the experiment. The Digiflow software was used extensively in processing the videos and taking measurements (12). Thickness measurements were obtained from light attenuation experiments that required calibration using a glass wedge of known dimensions. This procedure is detailed extensively in previous studies (9, 10, 20).

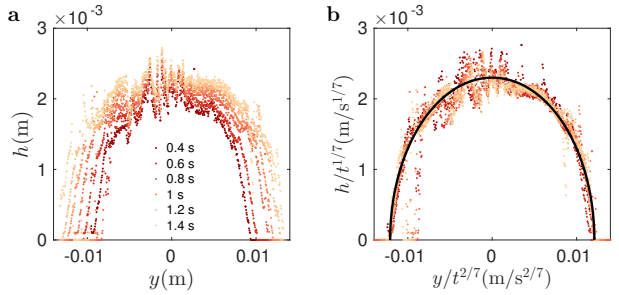

Fig. 6. Experimental measurements of the time evolution of the bridge height profile h in the y-z plane (Exp3): **a**, raw data; **b**, rescaled data using (3). The rescaled bridge heights collapse to a universal profile which has an elliptical shape (bold line). The noise in the data is from surface roughness along the bridge. The elliptic fit has a semi-major and minor radii of 1.2×10^{-2} and 2.3×10^{-3}, respectively.

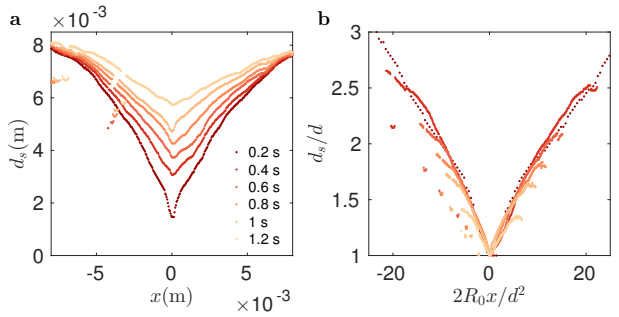

Fig. 7. Experimental measurements of the time evolution of the fracture profile on the x-y plane following the coalescence of two fractures (Exp1): **a**, raw data; **b**, rescaled data. The rescaled profiles, according to $b \approx d^2/2R_0$, collapse to a universal shape near the minimum in **b**, which suggests a local self-similar dynamic behaviour during the coalescence of two fractures.

Velocity field. Velocity field information was obtained from PIV experiments. A light sheet of approximately 10 mm was created using two arc lamps and slits on the side of a blacked out chamber holding the hydrogel. The fracturing fluid was then seeded with particles of diameter 40μm (Orgasol). The particles within the fracture were then illuminated with the light sheet and tracked using a PIV algorithm. The Digiflow software was used to calculate the corresponding velocity measurements (12). A small amount of fluorescein was also added to the fluid so that the fracture edge could be distinguished, but not so much that the light off the particles was saturated. The representative flux Q in Fig. 4, is calculated using $Q \approx \langle u \rangle 2dh$. Since no h measurements are available from PIV experiments, it was estimated using the experimental parameters and the pre-factor obtained from the fit in Fig. 5d.

Table 1. Experiments conducted with particular values of physical parameters.

Exp	l_0(mm)	E(kPa)	μ(Pa·s)	Q_0(mL/min)	γ_s(Jm^{-2})
Exp1	40	97	1.13	5.0	5.2
Exp2	40	97	1.13	2.0	5.2
Exp3	40	125	1.13	20	4.4
Exp4	35	125	0.28	10	4.4
Exp5	35	320	0.66	20	3.6
Exp6	40	97	0.44	5.0	5.2
Exp7	35	157	0.35	5.0	5.2
Exp8	30	125	0.37	5.0	4.4

ACKNOWLEDGMENTS. We would like to thank the technicians in the G.K. Batchelor lab for their help in setting up the experiment. This work was funded with the support of an iCASE award from the EPSRC and BP (Grant No. EP/L505389/1).

1. Economides MJ, Nolte KG (2000) Reservoir stimulation, vol 18. Wiley Chichester
2. Fairhurst C (1964) Measurement of in-situ rock stresses. With particular reference to hydraulic fracturing. Rock Mechanics (United States)
3. Rudnicki JW (2000) Geomechanics. International journal of solids and structures 37:349–358
4. Murphy HD, Tester JW, Grigsby CO, Potter RM (1981) Energy extraction from fractured geothermal reservoirs in low-permeability crystalline rock. Journal of Geophysical Research: Solid Earth 86:7145–7158
5. Lister JR, Kerr RC (1991) Fluid-mechanical models of crack propagation and their application to magma transport in dykes. Journal of Geophysical Research: Solid Earth 96:10049–10077
6. Mair R, Hight D (1994) Compensation grouting. World Tunnelling and Subsurface Excavation 7:361–367
7. O'Keeffe NJ, Huppert HE, Linden PF (2018) Experimental exploration of fluid-driven cracks in brittle hydrogels. Journal of Fluid Mechanics 844:435–458
8. Lai CY, Zheng Z, Dressaire E, Wexler JS, Stone HA (2015) Experimental study on penny-shaped fluid-driven cracks in an elastic matrix. Proceedings of the Royal Society A: Mathematical, Physical and Engineering Science 471:2182
9. Lai CY, Zheng Z, Dressaire E, Stone HA (2016) Fluid-driven cracks in an elastic matrix in the toughness-dominated limit. Philosophical Transactions of the Royal Society of London A: Mathematical, Physical and Engineering Sciences 374:2078
10. O'Keeffe NJ, Linden PF (2017) Hydrogel as a Medium for Fluid-Driven Fracture Study. Experimental Mechanics 57:1483–1493
11. Savitski AA, Detournay E (2002) Propagation of a penny-shaped fluid-driven fracture in an impermeable rock: asymptotic solutions. International Journal of Solids and Structures 39:6311–6337
12. Dalziel SB (2006) Digiflow user guide. DL Research Partners
13. Xiao ZM, Lim MK, Liew KM (1994) Stress intensity factors for two coplanar penny-shaped cracks under uniaxial tension. International Journal of Engineering Science 32:303–311
14. Paulsen, JD and Carmigniani, R and Kannan, A and Burton, JC and Nagel, SR (2014) Coalescence of bubbles and drops in an outer fluid. Nature Communications 5:3182
15. Ristenpart WD, McCalla PM, Roy RV, Stone HA (2006) Coalescence of spreading droplets on a wettable substrate. Physical review letters 97:064501
16. Hernández-Sánchez JF, Lubbers LA, Eddi A, Snoeijer JH (2012) Symmetric and asymmetric coalescence of drops on a substrate. Physical Review Letters 109:1–5
17. Zheng, Z, Fontelos, MA, Shin, S, Stone HA (2018) Universality in the nonlinear leveling of capillary films. Physical Review Fluids 3:032001
18. Zheng, Z, Fontelos, MA, Shin, S, Dallaston, MC, Tseluiko, D, Kalliadasis S, Stone HA (2018) Healing capillary films. Journal of Fluid Mechanics 838:404–434
19. Spence DA, Sharp P (1985) Self-similar solutions for elastohydrodynamic cavity flow. Proceedings of the Royal Society of London A Mathematical and Physical Sciences 400:289–313
20. Bunger AP (2006) A photometry method for measuring the opening of fluid-filled fractures. Measurement Science and Technology 17:3237
21. Kanninen, MF, Popelar, CL (1985) Advanced Fracture Mechanics, Oxford University Press
22. Rice, JR (1968) Mathematical analysis in the mechanics of fracture. Fracture: an advanced treatise 2:191–311